**ORIGINAL PAPER**

# Characterization of shear zones in soft granular beds by means of a novel magnetic resonance imaging technique

Jing Wang[1] · Zohreh Farmani[2] · Joshua A. Dijksman[2] · Cindy Lübeck[3] · Oliver Speck[1,3] · Ralf Stannarius[1]

## Abstract
We introduce a new Magnetic Resonance Imaging technique to study the geometry of shear zones of soft, low-frictional and hard, frictional granular materials and their mixtures. Hydrogel spheres serve as the soft, low-frictional material component, while mustard seeds represent rigid, frictional grains. Some of the hydrogel spheres are doped with $CuSO_4$ salt to serve as tracers. A cylindrical split-bottom cell is sheared stepwise and the shear profiles are determined from the differences of tomograms after successive shear steps, using Particle Imaging Velocimetry and Particle Tracking Velocimetry. We find that the shear zone geometry differs considerably between soft grains submersed in water and the same material without the embedding fluid.

Jing Wang and Zohreh Farmani have contributed equally to this study.

✉ Jing Wang
  jing.wang@ovgu.de

✉ Zohreh Farmani
  zohreh.farmani@wur.nl

✉ Ralf Stannarius
  ralf.stannarius@ovgu.de

  Joshua A. Dijksman
  joshua.dijksman@wur.nl

  Cindy Lübeck
  cindy.luebeck@ovgu.de

  Oliver Speck
  oliver.speck@ovgu.de

1  Institute of Physics, Otto von Guericke University Magdeburg, Universitätsplatz 2, 39106 Magdeburg, Germany

2  Physical Chemistry and Soft Matter, Wageningen University and Research, Stippeneng 4, 6708 WE Wageningen, The Netherlands

3  Forschungscampus STIMULATE, Otto-Hahn-Straße 2, 39106 Magdeburg, Germany

## 1 Introduction

Granular matter responds to shear stress with a behavior quite different from that of liquids. In contrast to simple liquids which distribute the shear uniformly, granular matter develops shear bands, where the shear deformation is usually localized in narrow zones. The geometry of such zones depends on the material properties and the shear geometry in a complex way. A characterization of the grain displacements inside a sheared granular bed is thus of high interest, from a practical point of view as well as from the aspect of fundamental understanding of granulate physics. The shear characteristics of granular matter is also relevant in natural phenomena, e.g. in the formation of avalanches or the stability of geological faults. One of the interesting phenomena is the tendency to reduce the packing fraction in shear zones, described by Reynolds [1] already in 1886, and first studied quantitatively by Bagnold [2, 3].

In the present study, we will focus on the question whether ensembles of soft, slippery grains behave quantitatively or even qualitatively different from hard, frictional grains when they are sheared in the same geometries. The detection of shear zones inside 3D granular beds is often a nontrivial task. With few exceptions, granular matter is opaque and optical methods fail to visualize the reorganization of the grains in the bulk. When one wants to gain

access to the internal processes in a granular bed and at the same time avoid destructive methods such as excavation, a couple of imaging techniques are available [4]. In transparent material, one can use optical fluorescence imaging with a laser sheet [5–8].

While this technique is rather affordable and simpler than the competing tomographic methods, it has several limitations. One restriction is that the material has to be submersed in an index-matching fluid, and this may influence the shear characteristics. A much more elaborate and expensive imaging technique is X-ray Computed Tomography. One can scan a variety of materials with this technique, and scanners are available with different spatial resolutions from micrometer sizes to centimeters [9–16]. A recent review by Weis and Schröter can be found in Ref. [17]. This technique is quite efficient when one can resolve the individual particles and perform Particle Tracking (PTV) or Particle Imaging (PIV) Velocimetry. However, it is relatively complicated to label individual particles as tracers, even though this is in principle possible. The problem is that X-ray absorption and particle densities are rather closely related to each other. If one chooses tracers with the same size as the background material, but with different X-ray absorption, one usually has to deal with tracers of different weights and sedimentation may become an issue. A workaround can be hollow particles as tracers in a bed of filled particles with the same weight and outer diameter.

Magnetic Resonance Imaging (MRI) is an alternative method that exploits the nuclear magnetization of the material for imaging [18, 19]. MRI-visible objects can be imaged directly, if they contain liquids e. g. [20–24], or NMR-invisible grains can be immersed in an MRI-visible fluid, e. g. [25–27], so that they appear as "shadows" in the tomograms. In the present study, we expand the opportunities of MR Imaging by mixing Magnetic Resonance visible grains with magnetically invisible grains of practically identical mechanical properties. This is achieved by a special preparation technique described in Sect. 2.2.

While MRI has a number of drawbacks compared to X-ray CT, one of the advantages is the opportunity to have tracers with practically the same physical properties as the bulk material except for the MRI visibility. This can be achieved either by using liquid-filled vs. solid particles, or, as in our experiments, by doping an amount of tracers. This technique allows us to monitor the displacement of the material inside the granular bed with PIV or PTV. Nuclear magnetic resonance can be used to reveal the inner structure of a granular bed either by packing density profiles [20, 28], or even at the grain level [27, 29]. Both MRI and X-ray CT are comparably slow methods, so that typically real-time imaging is not possible. There are some exceptionally fast techniques that allow the real-time imaging

at least of slices inside the granular bed, for example with MRI [23, 24, 30] and X-ray CT [16, 31, 32].

In the present study, we analyse displacements of grains in shear experiments. With the equipment and imaging method used in this study, the time to record one tomogram is about one minute. During the data acquisition, the granular ensemble has to be at rest. Thus, the sample is sheared in steps and MRI tomograms are recorded after each step in the static sample.

Two principal geometries can be employed to study shear of granular materials. Linear shear cells have a simple geometry, but they limit the displacement and are therefore suited only for oscillatory shear [7, 33]. In one study, long linear sliders were used to determine the distortion and reflexion of shear zones at the boundaries between layers of different granular materials [29]. For continuous shear experiments, closed shear zones in rotating systems are more suitable. Plate-plate or cone-plate geometries are preferentially used, where rheological problems like the shear rate dependence of the material is a focus [34, 35]. For the investigation of both transient and asymptotic states of shear zones, cylindrical split-bottom containers have proven advantageous [28, 36–39]. An inner, rotating granular volume is sheared relative to an outer, fixed volume. Earlier investigations have dealt with the geometry of the shear zone [36–42], dilatation of the shear zone [13, 28], alignment of shape-anisotropic grains under shear [12, 13], or the formation of surface heaps and secondary flows [43, 44].

These previous shear investigations exclusively dealt with frictional, hard particles. In the present study, we investigate the role of softness and slipperiness on the shear characteristics. We employ hydrogel spheres which are characterized by a very weak elastic modulus of the order of 10 kPa and a friction coefficient that is more than one order of magnitude smaller than for typical granular materials[45]. It has been demonstrated earlier that during silo discharge, hydrogel spheres behave qualitatively different from hard, frictional grains. Some features resemble rather liquid behavior that that of hard grains, for example, the pressure is almost hydrostatic over a substantial granular bed height. In addition to the pure material, we prepare mixtures of these soft grains with hard, frictional spheres in order to quantify the influence of the mixing ratio on the shear characteristics. We test whether the shear characteristics changes qualitatively when the admixture of hard, frictional spheres reaches a certain percolation threshold so that chains of these particles traverse the sheared regions.

## 2 Experimental setup and materials

### 2.1 Setup geometry

In order to keep the setup small enough to be inserted in the MRI scanner, the decision was made to use a split-bottom

cylindrical shear geometry. Figure 1 is a sketch of the cell used in our experiment. It is manufactured from acryl glass (Perspex) which is MRI invisible. The inner disk can be rotated by hand from the top, via the rod that connects to the bottom disk. The rotation speed was not particularly controlled. It was of the order of $\approx 30°/s$, and definitely not faster than that. This rotation rate is considered slow enough to justify the assumption that it plays no measurable role for the particle displacements.

The rotation angle is measured by a goniometer, which is fixed on the top sealed cover of the shear cell. In addition, two MRI-visible tracers (doped hydrogel hemispheres) are glued to the bottom of this disk so that the position and rotation state of the container can be directly retrieved from the MRI tomograms. The inner diameter of the container is $D_0 = 2R_0 = 150$ mm, and the rotating disk has a diameter of $D = 2R_s = 95$ mm.

The geometry and width of the shear zone depends on the ratio $H/R_s$ of the filling height $H$ and the radius $R_s$ of the rotating bottom plate [28, 37–41]. At small fill heights, ($H < 0.6\,R_s$), it was found for rigid, frictional spherical grains that the shear zone passes the granular bed completely as shown in Fig. 1 and the inner part of the granular material rotates synchronously with the bottom. When the fill height becomes larger and the axial rod shown in Fig. 1 is missing, the shear zone closes in and at sufficient heights it forms a closed dome above the bottom disk. In our experiment, the

geometry is slightly different (albeit, as we will show, with little consequences on the shear profile) because of the narrow central rod that is used to turn the bottom disk.

The MRI scanner used was a 3 Tesla Siemens MAGNETOM Skyra at the *STIMULATE* Forschungscampus Magdeburg with 70 cm bore size and short magnet. The tomograms have a voxel resolution of $0.75 \times 0.75 \times 0.7$ mm$^3$. Recording of a single tomogram took about 1 minute, and the setup was kept in a static condition during the recording. The acquisition time $\tau$ was of the order of a few ms, which is very short compared to the transversal relaxation time $T_2 > 1$ s of pure water. $T_1$ of water is about 3 s in our experiments.

## 2.2 Material

The soft, low-frictional material used in our experiments are hydrogel spheres (HGS). Two sizes of hydrogel spheres were studied, small ones and large ones (see Table 1). The dry powder of the small HGS (type "snow") was received from *JRM Chemical, Cleveland, USA* in a polydisperse mixture with diameters from a few micrometers to about 0.5 mm. The dry grains were sieved to obtain a narrow size distribution between 0.3 mm and 0.355 mm. After swelling in distilled water, the grains reached diameters between 2 mm and 3 mm.

In some experiments, we employed large HGS. The dry particles were also obtained from a commercial supplier (*Happy Store, Nanjing, China*). They were swollen in a mixture of distilled water and NaCl. The salt concentration determines the final diameter of the hydrogels. It was chosen such that the diameter was approximately 7 mm, with a polydispersity of about 5 %.

In addition, we used mustard seeds as hard, frictional grains in mixtures with the small HGS of comparable size. In principle, the swollen hydrogel spheres as well as the mustard seed contain liquids and provide a $^1$H NMR signal. However, because of the fast repetition rate of scans in our experiments, the recovery of the nuclear magnetization between subsequent scans is very small and the signal is weak due to the long $T_1$. This is a desired effect in our experiment, since we are interested to (i) keep the experiment time short and (ii) use specially prepared tracers. The
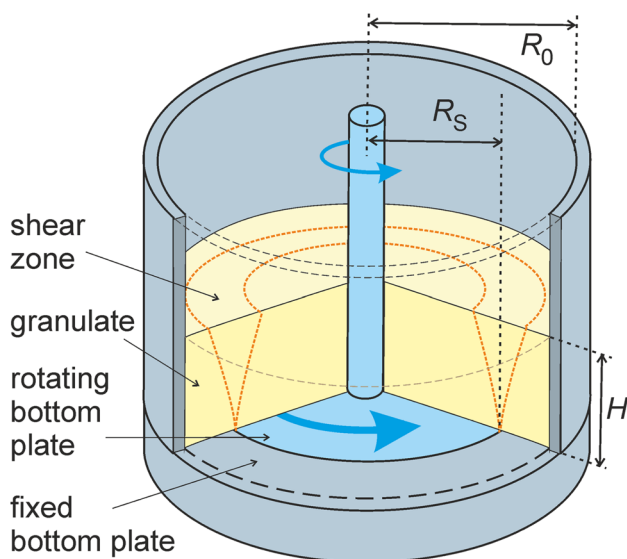


**Fig. 1** Sketch of the experimental setup: Grey parts are fixed in the MRI scanner, while bottom disk and central rod sketched in light-blue can be rotated about a vertical axis by well-defined steps. The granular material in the outer parts remains static and fixed to the outer container, while in the axial part it rotates with the bottom disk. The bottom surface was roughened in order to prevent the first layer to slide relative to the borders. The dashed lines sketch the boundaries of the shear zone

**Table 1** List of materials used

| Material | Mean diameter (mm) | Mean weight (mg) |
|---|---|---|
| Large hydrogel spheres | 7 | 180 |
| Small hydrogel spheres | 2.5 | 8 |
| Mustard seeds | 3 | 15 |

tracers are hydrogel particles that are swelled with an 8 mM aqueous solution of $CuSO_4$. The copper sulfate reduces the longitudinal relaxation time $T_1$ of the nuclear magnetization substantially [46]. Thus, the hydrogel particles swollen in the dopant solution produce a strong MRI signal. On average, we have used a share of about 20 % of doped hydrogels spheres in the experiments if not stated otherwise. After the particles were filled into the shear cell, the bottom plate was rotated in order to achieve an axially symmetric distribution.

## 2.3 Data evaluation

We observed that the swelling of the large HGS in $CuSO_4$ solution led to an unexpected effect right after swelling: the outer shells (about 1-2 mm) of the 7 mm hydrogel spheres became visible in the MRI tomograms, while the inner part was swollen but remained invisible in the tomograms (Fig. 2). These particles can be easily tracked in subsequent tomograms of sheared samples. For the small HGS, the chosen spatial resolution of the tomograms is at the limits when individual spheres are traced, but with a PIV technique it is easy to track the displacement of local particle configurations.

Figure 2 shows a slice of a test tomogram recorded with large hydrogel grains. The view is a horizontal cross section of a cylindrical container with four compartments. The sector on the left is filled with 7 mm HGS swollen in NaCl solution. The NMR signal is very weak because $T_1$ is much larger than the repetition rate of the scans, so that the nuclear magnetization does not recover between the scans. In the contrast enhanced image (middle), their weak signal is seen. In the bottom sector of the Figure, 7 mm HGS doped with copper sulfate are contained. They provide a strong NMR signal in their outer shell. The selected slice cuts the

hydrogels spheres in different positions, therefore the rings seen in the slice have different diameters. This shell-type tomographic pattern of single spheres remained even after one week. The copper sulfate requires several weeks to diffuse into the sphere center and to provide an MRI signal of filled spheres with our technique. Note also that, since the HGS in the bottom compartment were surrounded by air, the susceptibility mismatch led to artifacts that let the spheres appear rugged. The individual spheres are nevertheless clearly separated. In the right sector, the same doped spheres were submerged in distilled water. This removes the susceptibility mismatch artifacts completely. Each grain can be clearly identified.

Figure 2 (right) shows the same sample after several months. The spheres appear filled now. Obviously, the copper sulfate has diffused inside the spheres. Within the present study, we have not tested the dynamics of this process. It requires between a few weeks and several months.

Before we describe our shear experiments with hydrogel spheres in detail, we note that the slow diffusion of the $CuSO_4$ into hydrogel particle cores during the swelling process provides a unique tool when one is interested to scan ensembles of irregular grains. During the first days after the swelling process, only the outer borders of the grains are NMR-visible. In order to demonstrate this, We scanned centimeter-sized irregular, but nearly cube-shaped hydrogel blocks (GB-740, *Educational Innovations, Bethel CT, USA*). Different percentages of them (100% and 30%) were 8 mM $CuSO_4$ doped. The swelling process took 24 hours, and the MRI scans were performed 5 days after swelling. The 2D cross sections of tomograms in Fig. 3 confirm that the $CuSO_4$ decorates only zones at the surface of the blocks, in a similar way as the spherical hydrogels (Fig. 2). This makes the individual blocks visible in the scans. If the
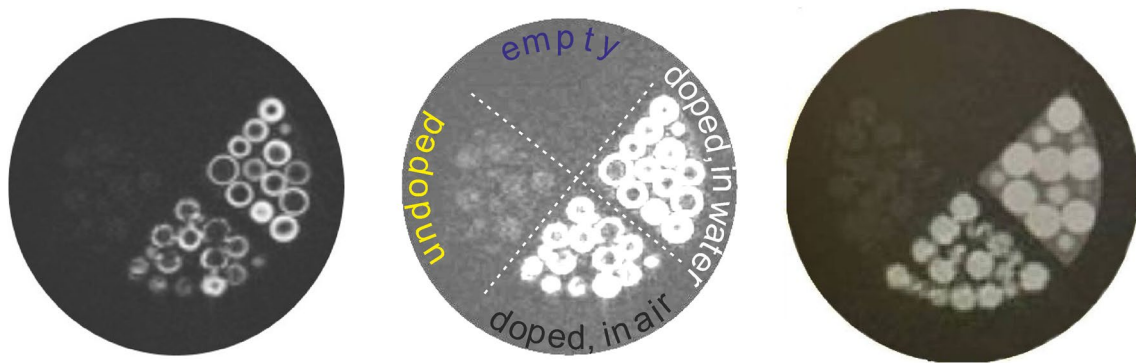


**Fig. 2** Left: Horizontal slice of the tomogram of a four compartment cylindrical plastic container (50 mm inner diameter) with large (7 mm) hydrogel spheres. The top sector is empty. The left sector contains non-doped spheres, swollen in NaCl solution. The bottom sector contains spheres doped with copper sulfate, and the right sector is filled with the same spheres submerged in distilled water. Middle: strongly contrast enhanced image of the same slice, which also shows the signal from undoped HGS (in the left sector). Right: Same sample as in the top right image, after 5 months. The $CuSO_4$ doped spheres are now completely visible, they appear as solid spheres in the tomograms, not as shells

complete hydrogel material would be NMR visible, blocks lying side-by-side would hardly be distingushable. When we decrease the share of doped particles in the packing (Fig. 3b) we only see the doped blocks (30%). One can easily track the doped blocks by segmenting the doped ones, as they are visible through edges. We conclude that this method can be extended successfully to any shape of hydrogel particles.

Typical reconstructions of the grains in our shear cell are shown in Fig. 4. Image (a) is a reconstruction of the large HGS ensemble with the doped tracers bright(yellow) and the non-doped background particles dark (blue). Image (b) shows the small HGS with the bright tracers and a dark background of voids and non-doped spheres.

In the shear experiments with large hydrogel spheres, we employ PTV to determine shear zone profiles from the traces of the doped particles. The concentration of these tracers is low enough so that they can be easily identified and collated in subsequent tomograms. The bottom plate was rotated in steps of $\approx 30$ degrees, and the tracer displacements between these shear steps were measured. To monitor the actual rotation angle, two tracers were glued below the rotating bottom plate. Their positions in the tomograms were used to confirm the correct position of the setup in the scanner and to determine the exact actual rotation angle of the bottom disk.

The assumptions implicitly made in this approach are that (1) the shear zone has axial symmetry around the central axis, and (2) that the initial transients after filling the container have ceased. The measurements show that after approximately 30 degrees of rotation of the bottom disk, a stationary profile of the shear zone is established. The 3D tomograms were divided into rings with constant height $h$
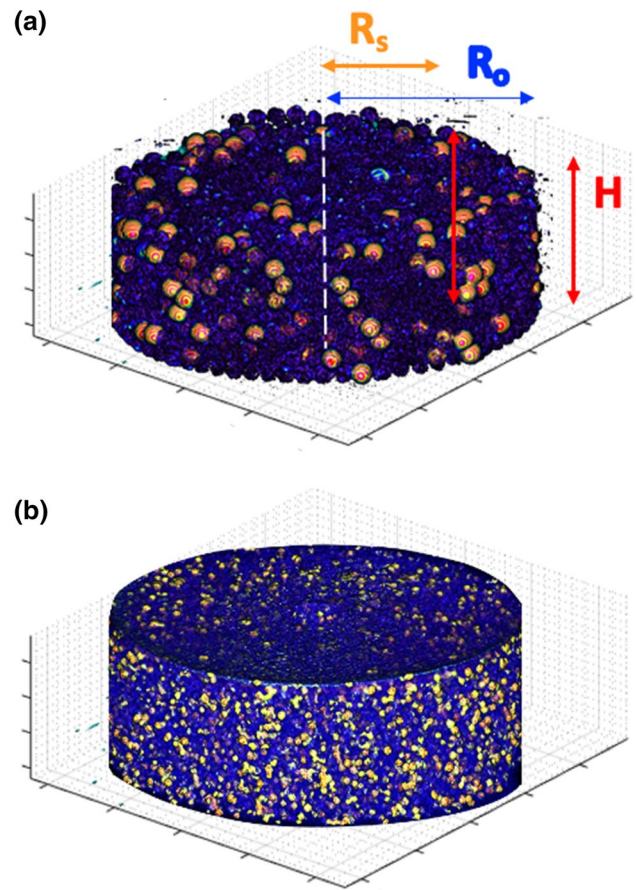


**(a)**

**(b)**

**Fig. 4** Typical examples of reconstructed 3D images of large (**a**) and small (**b**) hydrogel sphere ensembles. Copper sulfate doped particles appear bright in the dark (blue) background. The sample size is 15 cm in diameter
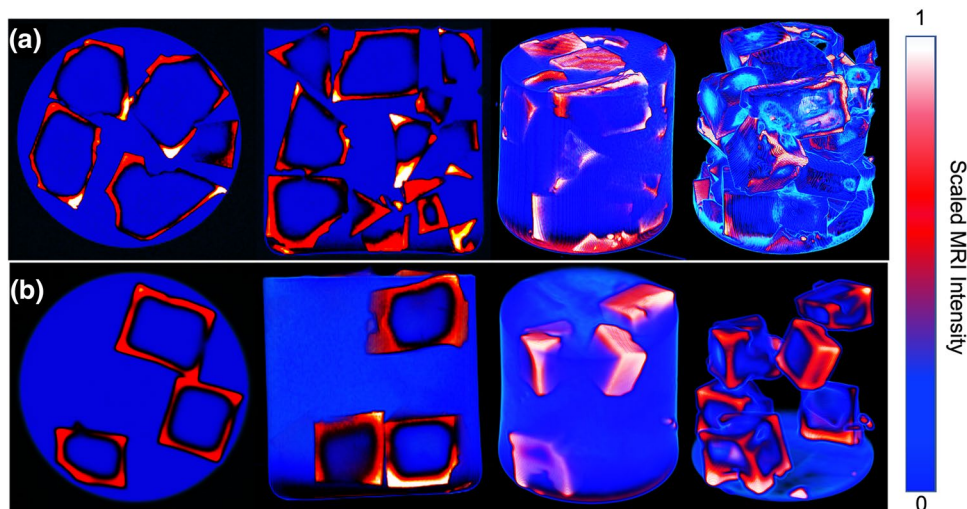


**Fig. 3** Nearly cube-shaped hydrogel blocks freshly swelled in 8 mM copper sulfate solution. **a** all hydrogel blocks labeled with $CuSO_4$, **b** only 30% of the blocks labeled. From left to right we show a central 2D horizontal slice, a 2D central vertical slice, 3D rendering and 3D rendering with water outside the cubes removed. Red to white regions label thin surface regions of the particles. Blue regions (low NMR signal) are further inside the blocks and around them. The container is a cylinder of 100 mm diameter, filled to a height of $\approx 95$ mm. MRI intensities are scaled by the maximum value

above the bottom and constant distance $r$ from the central axis. We average over $5 \times 5$ tomogram pixels (approximately $3.5 \times 3.5$ mm$^2$ in the $(h, r)$ plane. In each ring, the tangential displacement of doped grains was determined. The angular displacements of the tracers were scaled with the rotation angle of the bottom disk. Each experiment consisted of 7 to 11 evaluated shear steps of about 30 degrees. The data of these steps were averaged for each given fill height. In order to avoid influences of a transient behavior, the initial shear step was excluded. The advantage of this method is that the displacements can be determined with high precision for each doped grain, a disadvantage is the comparably poor spatial resolution of this method which is of the order of the HGS particle diameters. The choice of 30 degree rotation steps is a compromise. Too small rotation steps reduce the accuracy of the displacement vectors, while too large rotation steps can lead to a loss of particles between subsequent tomograms in a given ring, when the particle changes its radial or vertical position.

With the small grains, the same experimental steps were performed: stepwise slow rotations of the bottom plate by 10°. In these experiments, we did not follow individual grains but employed PIV to retrieve displacements in different zones of the granular bed. This results in a better spatial resolution because of the smaller particle diameters. The tomogram data of image pairs are sampled within rings of constant height above the bottom plate and equal distance from the rotation axis, and the spatial cross-correlations are calculated, providing the average azimuthal displacement at that height and radius.

## 3 Results

### 3.1 PTV of large grains

Figure 5 was constructed from horizontal slices of tomograms recorded in a 20 mm high layer of large HGS in our setup. One tomogram was taken after filling the container, then, the inner disk was rotated by nominally 30° and a second tomogram was recorded. From the displacement of the markers at the bottom of the rotating disk, the actual rotation angle was established to be precisely only 27°. The rotation speed was chosen sufficiently slow so that the sample was sheared quasi-statically. We can tacitly assume that the ratio of the angular displacement of a tracer at given radius $r$ and height $h$ and the angular displacement of the bottom disk is equal to the ratio $\omega/\omega_0$ of the angular velocities during slow, continuous shearing.

The first two images (a,b) show the overlay of identical slices of the two tomograms in pseudocolor: The green color plane of one slice was replaced by the green color plane of the second slice, while the red and blue color planes

remained unchanged. White spots in image (a) indicate tracer spheres that have not changed their positions, dark grey spots represent the background of non-doped spheres and light grey (green and magenta) spots are particles that have been displaced. They mark the differences of both tomograms. Positions of tracers in the 0° tomograms are reproduced in magenta, those in the 27° tomogram in green. For selected grains, the mapping of grain positions in the two tomograms are indicated by arrows that represent the displacement. In (a), the difference between the original, non-rotated tomograms is shown. The outer grains remained at their original positions, while the grains in the center have rotated with the bottom disk. The inner dashed circle marks the position of the edge of the rotating disk. The slice shown is located at $h = 10$ mm above the bottom, in the middle of the granular bed.

In (b), we have digitally rotated the second tomogram backwards by the rotation angle of the bottom disk. Now, white stands for particles that co-rotate with the bottom disk. Indeed, the marked particles in the inner part coincide, which indicates that they rotated in the laboratory frame by the same angle as the bottom disk. The bottom two slices (c,d) in the figure show the same overlays with tomograms recorded at 210° and 240° rotation angles. At these rotation angles, we expect that a stationary shear zone has established. A comparison of the positions of large HGS tracers (see, e. g., Fig. 5) confirms that all tracers located at similar heights and distances from the rotation axis are displaced by approximately the same angle.

The complete shear profile can be obtained by following the tracer positions in each ring of a given distance $r$ from the axis and height $h$ above the bottom by means of PTV, on a particle level. The result is shown in Fig. 6a. Here, we have determined the displacements of all marked grains in rings around the central axis, with a resolution of approximately one particle radius. The displacement angles were scaled with the rotation angle of the bottom disk. If one assumes that the ratio of angular displacements in a given height and radius is proportional to the rotation angle of the bottom disk, one can extrapolate the results to the effect of a continuous rotation. The ratio of rotation angles to the angle of the bottom disk can be assumed to be equal to the ratio of rotation speeds in a given $(h, r)$ zone to the rotation frequency $\omega_0$ of the bottom disk. In Fig. 6a, results for three different fill heights of the container were compiled, The top image is for a bed height $H \approx 20$ mm $(H/R_s = 0.42)$, the middle part for $H \approx 40$ mm $(H/R_s = 0.84)$, and the bottom image for $H \approx 50$ mm $(H/R_s = 1.05)$. The first layer of grains above the bottom disk rotates with that disk in all cases. In the shallow granular bed $(H = 20$ mm$)$ the shear gradient is almost completely horizontal everywhere, with a slight widening of the shear zone towards the top. With increasing bed height, the shear zone bends inwards (middle image of Fig. 6a).
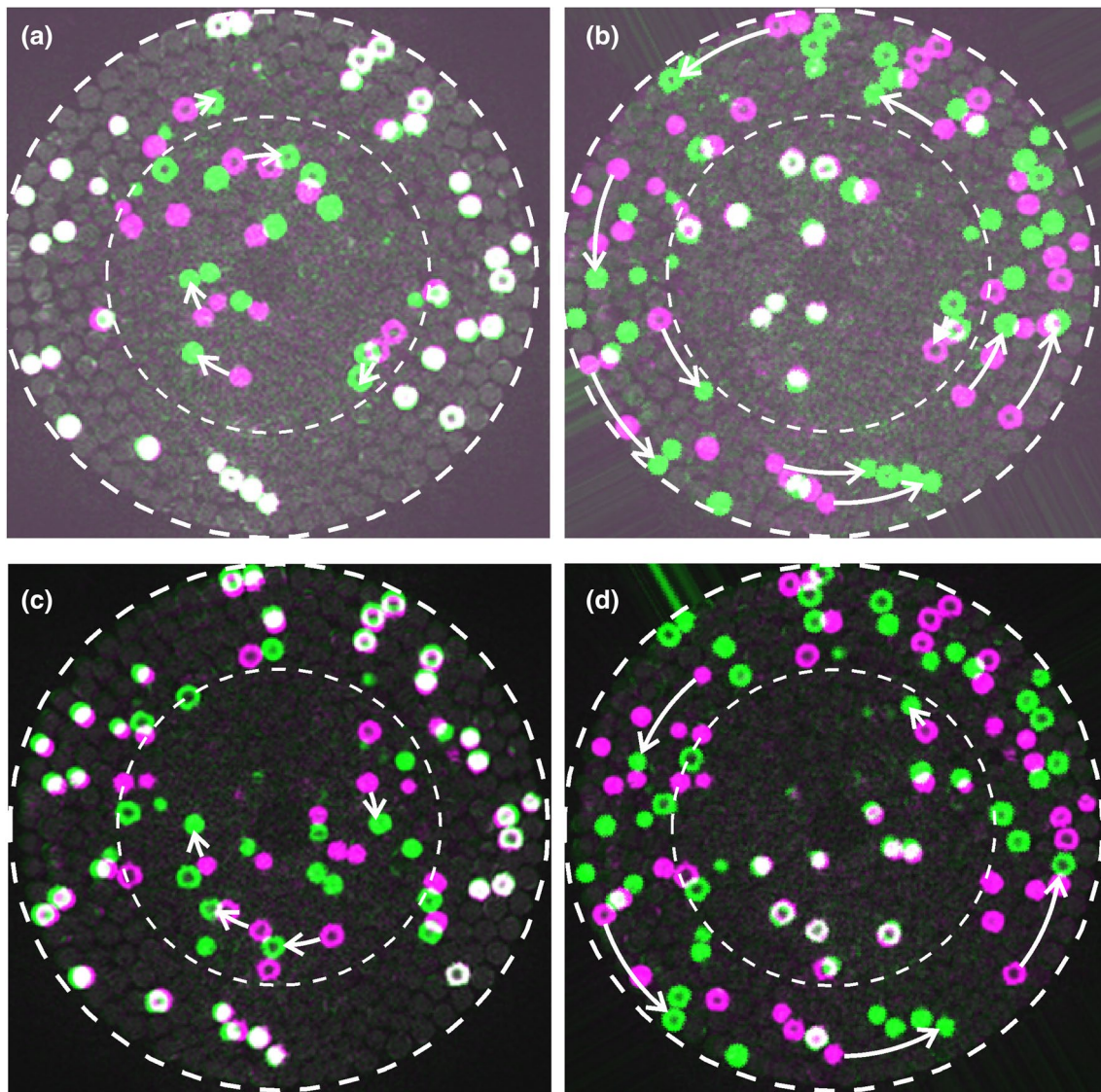
**Fig. 5** Displacement of large HGS during ≈ 30 deg rotations of the bottom plate. A horizontal slice at 10 mm height within a 20 mm high granular layer was selected. The dashed lines mark the inner of the container wall and the border of the rotating bottom disk. **a** shows in white the immobile tracers, in magenta the tracer positions after filling, and in green the displaced positions after rotation of the plate. Arrows indicate examples of selected displacements of individual tracers. **b** shows the differences in the frame of the rotating disk (disk rotation compensated by appropriate digital rotation of the slice), white tracers moved with the disk, magenta and green are tracers in the 0° and 27° tomograms, resp. **c,d** present the same operations with the same slice between the 210° and 240° rotations of the bottom plate

For the largest bed height studied in our MRI experiments ($H = 50$ mm), the shear zone is nearly vertical everywhere, confined to the first layer of HGS. Above a height of about 4 HGS diameters, the shear zone is confined to a narrow shell around the central rod that serves as the rotation axis of the bottom disk. In general, the PTV method is rather inaccurate for small $r$, near the central axis, because the displacement of tracers is very small there. Nevertheless, it is obvious from the tomogram data that the particles near the pole essentially follow the motion of the outer layers, the pole has little influence. This means, in particular, that for sufficiently large fill heights the closed dome-shape of the shear zone is almost the same as the one expected without a pole, with only small deviations in the lower part of the pole, near the horizontal dome. It is also noticeable that the shear zone for large fill heights above the bottom disk becomes rather sharp. This is a consequence of some lattice-like induced positional order of the spheres above the disk, in flat layers. Obviously, there is a sharp drop of the co-rotation with the bottom disk already above the second layer.

It is possible to establish the quantitative shape of the shear zone from these data, and Fig. 7 shows two examples.
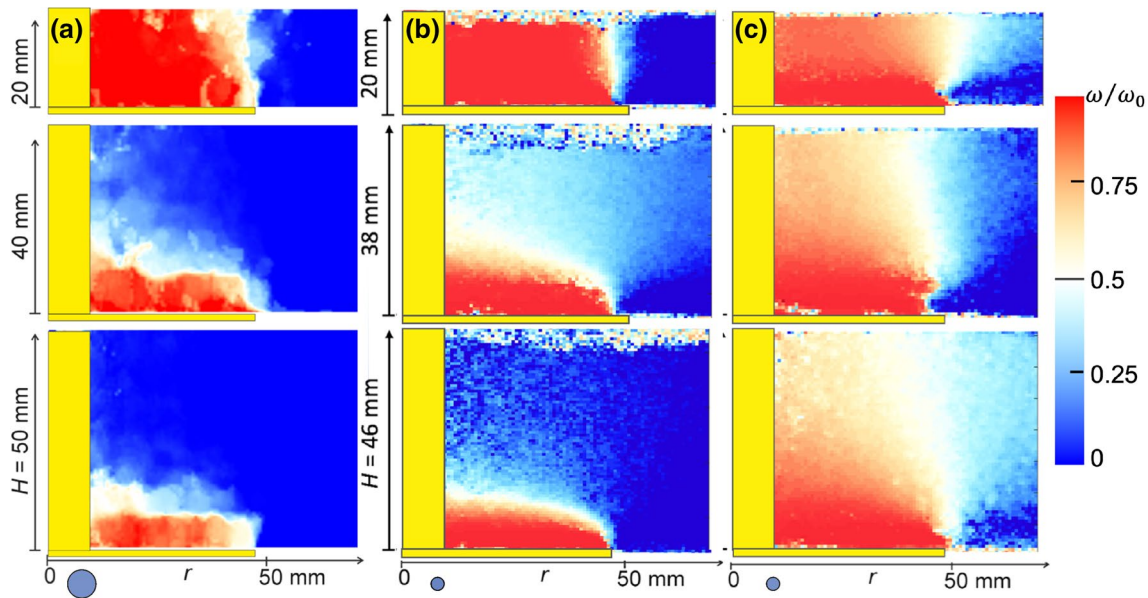
**Fig. 6** Flow profiles, **a** for large HGS (without immersion fluid), **b** for small HGS (without immersion fluid), and **c** for small HGS (grains immersed in water) in beds of different heights. Grey circles sketch the typical bead sizes. The vertical and horizontal yellow bars indicate the positions of the central rod and the bottom disk, respectively. The angular velocity $\omega(r, h)$ was normalized by the bottom disk angular velocity $\omega_0$. The shear zone where the angular velocity ranges between 0 and $\omega_0$ is visible as a bright band separating the grains at rest (outside) and co-rotating with the disk (center)

In the upper graph, the horizontal cut through the shear zone in the top layer is seen, a slice of five voxels height (3.75 mm) was averaged. The profile was fitted with a scaled complementary error function

$$\omega(r) = \frac{\omega_0}{2} \text{ erfc } (r) = \frac{\omega_0}{\sqrt{\pi}} \int_r^{\infty} \exp (-x^2)dx, \qquad (1)$$

using $x = (r - R_c)/\delta$ with the shear zone center radius $R_c$ and width $\delta$. The parameters are $R_C = 45$ mm, $\delta = 12.5$ mm in the top layer and $R_c = 47$ mm, $\delta = 7.5$ mm in the central layer. Note that $R_c$ is quite close to the bottom disk radius, as expected for this low fill height. This empirical function captures the profile satisfactorily well, and the parameters $\delta$ and $R_c$ may be used for a straightforward characterization of the shear zone width and position, in order to compare the influences of material parameters on the shear zone geometry. In more accurate experiments, we have focused on smaller spheres that are not equally well distinguished as single particles in our tomograms, and we have used PIV for the reconstruction of the shear profiles.

## 3.2 PIV of small grains

The study of the small HGS was performed in two parts. In the first part, the HGS were filled into the container after the water at their surfaces had been removed as thoroughly as

possible. Still, some excess water attached to the spheres was present, but in very small quantity, so that the voids between the spheres were filled almost exclusively with air. Then, the same experiments as with the large grains were repeated. We will call this condition a drained environment. The results are shown in Sect. 3.2.1. In another set of experiments, we filled the voids between the HGS in the shear cell with water. We will refer to this situation as "submersed" environment. Results will be discussed in Sect. 3.2.2.

### 3.2.1 Hydrogel spheres in air

Figure 6b shows the results for small HGS in the same fashion as Fig. 6a for the large HGS. It is obvious that the results look very similar to the large particle PTV results, with a slightly better spatial resolution in the PIV results for small HGS.

The PIV produces some artifacts in the surface layers of the granular bed. The reason is that small height differences in different regions are incorrectly interpreted by the correlation technique. If one disregards the upper 5 mm, there is a clear picture of the shear zone geometry: At low fill height, the shear zone reaches the top, and it is almost vertical, with a slight inclination inward towards the top layer. Above a certain fill height, the shear zone closes. The height of the dome-shaped shear zone approaches a saturation
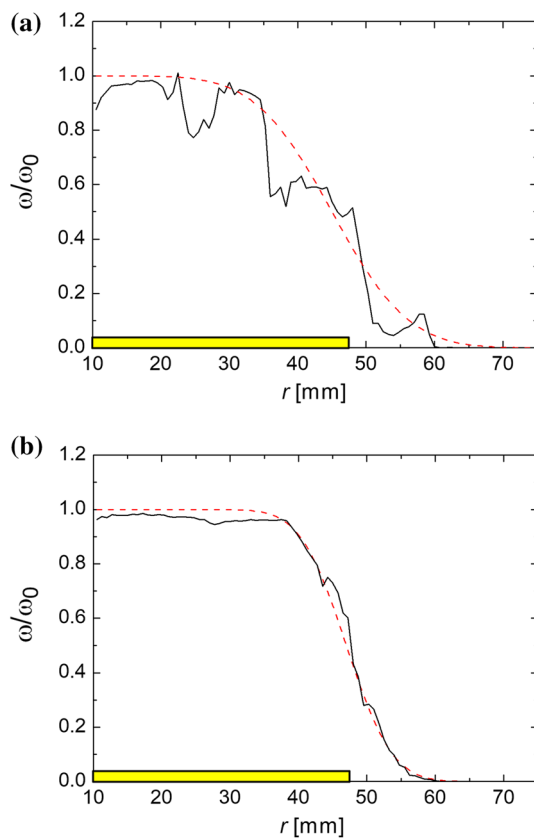
**(a)**



**(b)**



**Fig. 7** Shear profiles extracted from the $H = 20$ mm experiment with large grains. The graphs show the profiles (relative rotation speed in a ring of radius $r$ at height $h$ for $h = H$ (**a**) and $h = H/2$ (**b**). The profiles are averages of 6 angular difference measurements each. The parameters for the erfc-graphs (dashed lines) are given in the text. The horizontal bars indicate the position of the rotating bottom disk

value. When $H \approx R_s$, it reaches about $0.2\,R_s$. These results are qualitatively similar to results of earlier studies of rigid, frictional grains.

### 3.2.2 Hydrogel spheres immersed in liquid

In the second set of experiments, tomograms were recorded with submersed HGS. The density of the HGS is a few percent higher than that of water so that the buoyancy compensates approximately 95% of the weight. This reduction of the effective weight also compensates the contact forces between the grains. Yet this is not the only effect that has to be considered: The water filling the voids between the small grains removes capillary forces that presumably exist in the dry environment because the HGS surfaces are not completely dry, and liquid bridges can form between touching spheres. Thus, one may expect a reduced friction force. Finally, the embedding water has to be redistributed when the grain ensemble is sheared. This involves the inner

friction of the fluid and may lead to a more liquid-like shear characteristics in our material.

The MRI results are shown in Fig. 6c. The presence of interstitial water does not affect the MRI spectra because it gives an equally weak signal as the HGS swollen in pure water. The shear zone is much broader for all fill heights. As in the dry experiment, the central region that rotates with the bottom disk extends to the top layer at heights up to $H \approx 0.4R_s$, but then, with increasing bed height, the shear zone does not close dome-like above the disk. Even when the bed height $H$ is comparable to the disk radius, the top layers react to the disk rotation, although with a reduced rate. The shear profile is qualitatively different from that of the dry material. This is in a way somewhat counter-intuitive, since a reduced effective weight leads to lower vertical contact forces and one would perhaps assume that the transmission of shear forces in the vertical direction is reduced.

### 3.2.3 Mixtures of hard frictional and soft, low-frictional grains

In the third set of experiments, the HGS were mixed with rigid frictional mustard seeds of comparable sizes in different mixing ratios. Here, the experiments were restricted to a single fill height, 15 mm. Within our experimental limits, we cannot see a clear difference in the flow profiles of the rigid pure mustard seed sample and the pure soft, low-frictional HGS sample (see Figs. 6a,b and 8, top). This is, at first glance, an astonishing observation in view of the fact that the outflow of HGS from hoppers was found to be qualitatively different from that of hard, frictional grains [47, 48]. We will discuss the differences between the two experiments below in Sect. 4.2. On the other hand, the shear zones of the mixtures are wider than those of the pure materials. This could be an indication that introducing "soft spots" in a bed of hard grains may increase fluctuations and the propagation of strain.

## 4 Discussion

### 4.1 Methodical achievements

We have demonstrated that shear profiles in soft particle ensembles can be measured by means of a non-invasive Magnetic Resonance Imaging approach. The displacement of particles was determined from differences of tomograms after stepwise rotation of the bottom disk in a split-bottom container. Two techniques have been employed to extract the particle displacements during the discrete shear steps. The first method was used for the large HGS. The positions of individual marked tracers in given heights $h$ and radii $r$ were evaluated and a displacement profile was derived. The
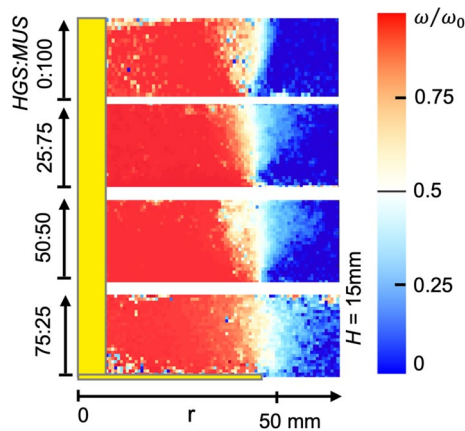
**Fig. 8** Shear zone profiles for small HGS mixed with rigid, frictional mustard grains in different concentrations. The vertical and horizontal bars indicate the positions of the central rod and of the bottom disk, respectively. The plot shows the ratio of the displacement angles of grains at ($h$, $r$) and scaled by the rotation of the bottom disk. No immersion fluid was present.The yellow bars in the figure indicate the positions of the central rod and of the rotating inner plate

method requires that in each ring ($h$, $r$), at least one tracer is found. This condition was fulfilled with tracer concentrations between 10% and 20%. The method is comparable to an earlier investigation of shear profiles in linear sliders [29] where poppy seeds distributed in beds of glass spheres and corundum grains were tracked. The advantages of the method applied in this study over the earlier system are twofold. First, we can strictly exclude segregation in the pure HGS systems, since the tracers are identical in their physical properties to the non-marked background particles. Second, doping with copper sulfate substantially reduces the recording time of the images.

The second approach, PIV, was used for the small HGS. The correlations of tomogram profiles in rings of constant ($h$, $r$) provided the mean displacements in each ring, which were used to construct the displacement profiles. This method averages over the whole ring and it is therefore less suited to probe possible variations of the shear zone along an azimuthal cut. However, it provides a much better spatial resolution than the PTV of large grains.

Of course, PTV can in principle also be used in small particle ensembles (e.g. Ref. [29]) as long as the individual grains can be identified. Then, however, much smaller shear steps (of the order of 5° rotations) are needed for a correct mapping of the individual grains. Then, one either loses relative accuracy of the angular displacements or much more tomograms need to be recorded.

We note that the investigation of hydrogel spheres of different sizes offers an, although limited, access to study the role of softness: The choice of particle diameters does not change the elastic modulus significantly, but the particle weight and thus gravitational as well as shear forces increase

with approximately the third power of the radius. Thus the hydrogel spheres behave more like hard, low-friction grains in small size experiments but more like soft, deformable low-frictional grains in larger size experiments, when the setup is appropriately scaled with the particle sizes.

An additional interesting feature of the specific labeling method of hydrogel particles that has been used here is the initial concentration of the $CuSO_4$ in the outer layers of the particles, irrespective of their particular shapes. The thickness of these layers is of the order of 1 mm within the first few days after swelling. This allows us to map particles by their borders. This feature is very helpful particularly when neighboring particles (e. g. polyhedra) touch each other with flat faces. If the labeling would make the complete particle visible in the tomogram, then such particles would be very hard to separate in the image data.

## 4.2 Shear zone characterization

An important result of this study is the characterization of the shear profiles in ensembles of soft, slippery materials. We find that there is little difference between the profiles in mustard seed ensembles, as representatives of hard, frictional spheres, and HGS ensembles (in dry environment) representing soft grains with very low friction. Mixtures of soft and rigid spheres do not show a clear trend.

At first glance, this finding of similar shear zone profiles of the HGS and mustard seeds contradicts findings in hopper outflow, where the flow in a quasi two-dimensional container was found to differ considerably between soft slippery, rigid frictional, and mixed systems. It was argued earlier that neither the softness nor the low friction alone cause the specific flow behavior [47–50], but a combination of both.

When comparing these results to the present experiment, one has to keep in mind that the gravitational pressure in the shear setup is considerably smaller than in the hoppers studied the above cited studies. The granular bed is much shallower in this MRI study. Thus, the softness of the spheres plays a less important role in the shear experiment. In the hopper, the bottom pressure is of the order of several kPa, and it can deform the spheres by up to 10% of their dimensions. In contrast, the gravitational pressure in the present shear cell hardly reaches 0.5 kPa, which has much lower effect on shape deformations of the HGS with elastic moduli of the order of 10 kPa. The other characteristic property of the HGS, their extremely low friction coefficient ($\mu$ of the order of 0.03) is, however, equally effective in the shear experiment reported here as in the earlier hopper experiments. Thus, the comparison of the flow characteristics of small HGS in a shallow bed with flow of larger HGS in higher beds can help to discriminate the influences of friction and elasticity.

At the contacts between HGS, liquid capillary bridges may form, and can in principle influence the shear behavior. However, a good argument to neglect these bridges is the comparison of Fig. 6a and b. There is little difference between the shear profiles of both kinds of particles. The masses of the particles in the study, however, relate like 22:1. For comparison, the bond numbers relating gravitational and capillary forces are of the order of one for the large hydrogel beads and roughly of the order of 0.1 for the small HGS. If capillary forces would influence the shear profiles, they would affect the small HGS much more than the large ones, and differences would become evident.

When the HGS in dry environment are compared with the submerged particles in the same geometries (Fig. 6b and c), considerable differences are evident. Since we have excluded the effect of capillary forces, the differences must be attributed to the shear of the interstitial liquid. The system of low-frictional HGS with interstitial fluid behaves more liquid-like, i.e. the shear zone tends to spreads across the cell. This behavior deserves a more detailed investigation in future experiments. It should be noted that we do not expect a similar effect with immersed frictional grains, at least at sufficiently low shear rates, because there, the shear forces will be primarily mediated by particle-particle contacts. With the low-frictional HGS, however, internal friction within the liquid may be of comparable influence as the direct particle contacts. A dependence of the ratio of these frictional forces on shear rates is expected. This should be done in rheological experiments by shear-rate dependent torque measurements.

Finally, the comparison of hard, frictional mustard seeds and soft HGS shows that both systems behave rather similar in dry environment. The mixtures of hard and soft grains appear to show a tendency to broaden the shear zones, which needs further exploration.

## 5 Summary

In this paper, we have introduced a new method to label tracers for MRI shear experiments with granular materials. It is based on a particular preparation technique for the hydrogel spheres that are studied. Copper sulfate added in very small concentration to the water in which the spheres are swelled reduces the longitudinal relaxation time $T_1$ of the nuclear magnetization well below that of pure water. At sufficiently fast acquisition rates of the MRI signal, the non-doped spheres are hardly visible in the tomograms while the doped particles provide a clear signal. At the same time, the physical properties of the marked particles are practically unchanged with respect to those swelled in pure water. This avoids any segregation of doped or non-doped particles in the ensemble during shear or flow experiments, which is a clear advantage over techiques where tracers have different physical properties from the other particles in the ensemble.

The method was employed to characterize shear zones in dry and submerged granular beds of hydrogel spheres and in mixtures of soft and hard grains of comparable sizes. A more comprehensive study of these systems with the technique introduced here is in progress.

## Declarations

**Conflict of interest** There are no conflicts to declare.

## References

1. Reynolds, O.: Experiments showing dilatancy, a property of granular material, possibly connected with gravitation. Proc. Roy. Inst. Great Britain **2**, 354–363 (1886)
2. Bagnold, R.A.: Experiments on a gravity-free dispersion of large solid spheres in a Newtonian fluid under shear. Proc. Roy. Soc. A **225**, 49 (1954)
3. Bagnold, R.A.: The shear and dilatation of dry sand and the 'singing' mechanism. Proc. Roy. Soc. A **295**, 219 (1966)
4. Amon, A., et al.: Preface: focus on imaging methods in granular physics. Rev. Sci. Instr. **88**, 051701 (2017)
5. Tsai, J.-C., Voth, G.A., Gollub, J.P.: Internal granular dynamics, shear-induced crystallization, and compaction steps. Phys. Rev. Lett. **91**, 064301 (2003)
6. Tsai, J.-C., Gollub, J.P.: Slowly sheared dense granular flows: crystallization and nonunique final states. Phys. Rev. E **70**, 031303 (2004)
7. Andreea Panaitescu, K., Anki, R., Arshad, K.: Nucleation and crystal growth in sheared granular sphere packings. Phys. Rev. Lett. **108**, 108001 (2012)

8. Dijksman, J.A., Brodu, N., Behringer, R.P.: Refractive index matched scanning and detection of soft particles. Rev. Sci. Instrum. **88**, 051807 (2017)

9. Richard, P., Philippe, P., Barbe, F., Bourlès, S., Thibault, X., Bideau, D.: Analysis by X-ray microtomography of a granular packing undergoing compaction. Phys. Rev. E **68**, 020301 (2003)

10. Zhang, W., Thompson, K.A., Reed, A.H., Beenken, L.: Relationship between packing structure and porosity in fixed beds of equilateral cylindrical particles. Chem. Eng. Sci. **61**, 8060 (2006)

11. Börzsönyi, T., Szabó, B., Törös, G., Wegner, S., Török, J., Somfai, E., Bien, T., Stannarius, R.: Orientational order and alignment of elongated particles induced by shear. Phys. Rev. Lett. **108**, 228302 (2012)

12. Wegner, S., Börzsönyi, T., Bien, T., Rose, G., Stannarius, R.: Alignment and dynamics of elongated cylinders under shear. Soft Matter. **8**, 10950–10958 (2012)

13. Wegner, S., Stannarius, R., Boese, A., Rose, G., Szabo, B., Somfai, E., Börzsönyi, T.: Effects of grain shape on packing and dilatancy of sheared granular materials. Soft Matter. **10**, 5157 (2014)

14. Szabó, B., Török, J., Somfai, E., Wegner, S., Stannarius, R., Böse, A., Rose, G., Angenstein, F., Börzsönyi, T.: Evolution of shear zones in granular materials. Phys. Rev. E **90**, 032205 (2014)

15. Stannarius, R., Sancho Martinez, D., Finger, T., Somfai, E., Börzsönyi, T.: Packing and flow profiles of soft grains in 3d silos reconstructed with X-ray computed tomography. Granular Matter **21**, 56 (2019)

16. Stannarius, R., Martinez, D.. S.., Börzsöny, T.., Bieberle, M.., Barthel, F.., Hampel, U..: High-speed X-ray tomography of silo discharge. New J. Phys. **21**, 113054 (2019)

17. Weis, S., Schröter, M.: Analyzing X-ray tomographies of granular packings. Rev. Sci. Instr. **88**, 051809 (2017)

18. Sederman, A.J., Gladden, L.F., Mantle, M.D.: Application of magnetic resonance imaging techniques to particulate systems. Adv. Powder Techn. **18**, 23–38 (2007)

19. Stannarius, R.: Magnetic resonance imaging of granular materials. Rev. Sci. Instr. **88**, 051806 (2017)

20. Nakagawa, M., Altobelli, S.A., Caprihan, A., Fukushima, E., Jeong, E.-K.: Non-invasive measurements of granular flows by resonance imaging. Exp. Fluids **16**, 54 (1993)

21. Nagakawa, M.: Axial segregation of granular flows in a horizontal rotating cylinder. Chem. Eng. Sci. **9**, 2540 (1994)

22. Sommier, N., Porion, P., Evesque, P., Leclerc, B., Tchoreloff, P., Couarraze, G.: Magnetic resonance imaging investigation of the mixing-segregation process in a pharmaceutical blender. Int. J. Pharmaceutics **222**, 243–258 (2001)

23. Penn, A., Boyce, C.M., Pruessmann, K.P., Müller, C.R.: Regimes of jetting and bubbling in a fluidized bed studied using real-time magnetic resonance imaging. Chem. Eng. J., 383: 123185, 10 (2019)

24. Penn, A.., Padash, A., Lehnert, M., Pruessmann, K., Müller, C., Boyce, C.: Asynchronous bubble pinch-off pattern arising in fluidized beds due to jet interaction: a magnetic resonance imaging and computational modeling study. Phys. Rev. Fluids **5**, 09 (2020)

25. Finger, T., Voigt, A., Stadler, J., Niessen, H..G., Naji, L., Stannarius, Ralf: Coarsening of axial segregation patterns of slurries in a horizontally rotating drum. Phys. Rev. E **74**, 031312 (2006)

26. Naji, L., Stannarius, R.: Axial and radial segregation of granular mixtures in a rotating spherical container. Phys. Rev. E **79**, 031307 (2009)

27. Fischer, D., Finger, T., Angenstein, F., Stannarius, R.: Diffusive and subdiffusive axial transport of granular material in rotating mixers. Phys. Rev. E **80**, 061302 (2009)

28. Sakaie, K., Fenistein, D., Carroll, T. J., van Hecke, M., Umbanhowar, P.: Mr imaging of reynolds dilatancy in the bulk of smooth granular flows. EPL (Europhys. Lett.) **84**, 38001 (2008)

29. Börzsönyi, T., Unger, T., Szabó, B., Wegner, S., Angenstein, F., Stannarius, R.: Reflection and exclusion of shear zones in inhomogeneous granular materials. Soft Matter **7**, 8330 (2011)

30. Engel, Maria, Kasper, Lars, Wilm, Bertram, Dietrich, Benjamin, Vionnet, Laetitia, Hennel, Franciszek, Reber, Jonas, Pruessmann, Klaas: Mono-planar t-hex: Speed and flexibility for high-resolution 3d imaging. Mag. Res. Med. **85**, 2507 (2020)

31. Bieberle, M., Barthel, F.: Magnetic resonance imaging of granular materials. Chem. Eng. J. **285**, 218 (2016)

32. Waktola, S., Bieberle, A., Barthel, F., Bieberle, M., Hampel, U., Grudzien, K., Babout, L.: A new data-processing approach to study particle motion using ultrafast X-ray tomography scanner: case study of gravitational mass flow. Experiments Fluids **59**, 03 (2018)

33. Panaitescu, A., Kudrolli, A.: Experimental investigation of cyclically sheared granular particles with direct particle tracking. Progr. Theor. Phys. Suppl. **184**, 100 (2010)

34. Kuwano, O., Ando, R., Hatano, T.: Crossover from negative to positive shear rate dependence in granular friction. Geophys. Res. Lett. **40**, 1295–1299 (2013)

35. Fall, A., Ovarlez, G., Hautemayou, D., Mézière, C., Roux, J.-N., Roux, J.-N., Chevoir, F.: Dry granular flows: rheological measurements of the $\mu$(i) -rheology. J. Rheology **59**, 1065 (2015)

36. Fenistein, D., van Hecke, M.: Wide shear zones in granular bulk flow. Nature **425**, 256 (2003)

37. Fenistein, D., van de Meent, J.-W., van Hecke, M.: Universal and wide shear zones in granular bulk flow. Phys. Rev. Lett. **92**, 094301 (2004)

38. Cheng, X., Lechman, J.B., Fernandez-Barbero, A., Grest, G.S., Jaeger, H.M., Karczmar, G.S., Möbius, M.E., Nagel, S.R.: Three-dimensional shear in granular flow. Phys. Rev. Lett. **96**, 038001 (2006)

39. Fenistein, D., van de Meent, J.-W., van Hecke, M.: Core precession and global modes in granular bulk flow. Phys. Rev. Lett. **96**, 118001 (2006)

40. Unger, T., Török, J., Kertész, J., Wolf, D.E.: Shear band formation in granular media as a variational problem. Phys. Rev. Lett. **92**, 214301 (2004)

41. Török, J., Unger, T., Kertész, J., Wolf, D.E.: Shear zones in granular materials: optimization in a self-organized random potential. Phys. Rev. E **75**, 011305 (2007)

42. Dijksman, J.A., van Hecke, M.: Granular flows in split-bottom geometries. Soft Matter **6**, 2901 (2010)

43. Wortel, G., Börzsönyi, T., Somfai, E., Wegner, S., Szabó, B., Stannarius, R., van Hecke, M.: Heaping, secondary flows and broken symmetry in flows of elongated granular particles. Soft Matter **11**, 2570 (2015)

44. Fischer, D., Börzsönyi, T., Nasato, D., Pöschel, T., Stannarius, R.: Heaping and secondary flows in sheared granular materials. New J. Phys. **18**, 113006 (2016)

45. Ashour, A., Trittel, T., Börzsönyi, T., Stannarius, R.: Silo outflow of soft frictionless spheres. Phys. Rev. Fluids **2**, 123302 (2017)

46. Kjaer, L., Thomsen, C., Henriksen, O., Ring, P., Stubgaard, M., Pedersen, E.J.: Evaluation of relaxation time measurements by magnetic resonance imaging. Acta Radiologica **28**, 345 (1987)

47. Harth, K., Wang, J., Börzsönyi, T., Stannarius, R.: Intermittent flow and transient congestions of soft spheres passing narrow orifices. Soft Matter **16**, 8013 (2020)

48. Wang, J., Harth, K., Stannarius, R., Fan, B., Börzsönyi, T.: Discharge of soft and hard grains and their mixtures from 2D silos. EPJ Web Conf. **249**, 03002 (2021)

49. Wang, J., Fan, B., Pongó, T., Harth, K., Trittel, T., Stannarius, R., Illig, M., Börzsönyi, T., Cruz Hidalgo, R.: Silo discharge of mixtures of soft and rigid grains. Soft Matter **17**, 4282 (2021)

50. Pongó, T., János, T., Stiga, V., Szabó, B., Lévay, S., Stannarius, R., Cruz Hidalgo, R., Börzsönyi, T.: Flow in an hourglass: particle friction and stiffness matter. New J. Phys. **23**, 023001 (2021)